### Title

Intentional carbon doping reveals CH as an abundant charged impurity in nominally undoped synthetic WS2 and WSe2




### Journal

2D Materials, 7(3)

### ISSN

2053-1583



### Authors

Cochrane, KA
Zhang, T
Kozhakhmetov, A
et al.



### Publication Date

2020-07-01

### DOI

10.1088/2053-1583/ab8543

Peer reviewed

# Intentional carbon doping reveals CH as an abundant charged impurity in nominally undoped synthetic $WS_2$ and $WSe_2$

**K.A. Cochrane[1*], T. Zhang[2,3], A. Kozhakhmetov[2], J.-H. Lee[1,4], F. Zhang[2,3], C. Dong[2,3], J.B. Neaton[1,4,5], J.A. Robinson[2,3], M. Terrones[2,3,6], A. Weber Bargioni[1*], and B. Schuler[1*]**

[1] Molecular Foundry, Lawrence Berkeley National Laboratory, California 94720, USA
[2] Department of Materials Science and Engineering, The Pennsylvania State University, University Park, PA 16082
[3] Center for Two-Dimensional and Layered Materials, The Pennsylvania State University, University Park, PA, 16802
[4] Department of Physics, University of California at Berkeley, Berkeley, CA 94720, USA
[5] Kavli Energy Nanosciences Institute at Berkeley, Berkeley, California 94720, USA.
[6] Department of Physics and Department of Chemistry, The Pennsylvania State University, University Park, PA, 16802

E-mail: kacochrane@lbl.gov,afweber-bargioni@lbl.gov,bschuler@lbl.gov

**Abstract.** Understanding the physical properties and controlling the generation of intrinsic and extrinsic defects is central to the technological adoption of 2D materials in devices. Here we identify a charged carbon-hydrogen complex at a chalcogen site ($CH_X$) as a common, charged impurity in synthetically grown transition metal dichalcogenides (TMDs). This conclusion is drawn by comparing high resolution scanning probe microscopy measurements of nominally undoped and intentionally carbon doped TMD samples. While CH impurity densities in undoped CVD-grown $WS_2$ and MOCVD-grown $WSe_2$ can range anywhere from parts per million to parts per thousand, CH densities in the percentage levels were selectively generated by a post-synthetic methane plasma treatment. Our study indicates that methane plasma treatment is a selective and clean method for the controlled introduction of a charged carbon-hydrogen complex at a surface chalcogen site, a defect that is commonly present in synthetic TMDs.

Submitted to: *2D Mater.*

## Introduction

Chemical doping is a vital technology to tune the transport and optoelectronic properties of semiconductors through band-gap engineering. In bulk materials, dopants are often introduced to create shallow defect states close to the band edges in order to generate mobile charge carriers. In contrast, dopants in two-dimensional (2D) materials such as transition metal dichalcogenides (TMDs) exhibit significantly more localized wavefunctions and higher binding energies deeper in the band gap [1–3]. This poses severe limitations to transferring the concept of chemical doping to low-dimensional material systems, but offers exciting possibilities to create surface-bound atomic quantum systems by chemical design rules [4, 5]. For both classical optoelectronic and quantum photonic applications, it is desirable to suppress the intrinsic disorder in 2D semiconductors to an absolute minimum. In particular, avoiding or passivating any deleterious defects that act as charge traps [6, 7], add to charge scattering [8] and recombination [9, 10], and cause decoherence effects by fluctuating magnetic fields [11] is an essential step for their technological adoption. [12–14] Hence, a detailed understanding of types and properties of impurities present in synthetically grown 2D materials is essential.

Previously we used a combination of different high-resolution scanning probe methods and *ab initio* calculations to identify common impurity defects in chemical vapor deposition (CVD)-grown tungsten disulfide ($WS_2$) such as oxygen substituting for sulfur ($O_S$), and chromium or molybdenum substituting for tungsten ($Cr_W$ or $Mo_W$). [15–17] Importantly, we established the correlation between the atomic structure and electronic properties of these defects. However, one defect that we commonly observed in our samples, we were previously not able to identify. [7,15] This defect is also consistently observed in other STM studies on a variety of TMDs and either left unidentified [18,19] or the assignment was ambiguous. [13,20,21] This defect is known to be negatively charged [7, 15, 19]. Charged defects can be detrimental to intrinsic 2D material functionality, for instance by acting as strong scattering centers limiting charge carrier mobility [6, 10, 22], or modifying luminescence by enhancing charge recombination [23] and shortening exciton lifetimes. [24,25] We recently found that the negative charge trapped at the defect site gives rise to a series of hydrogenic bound and resonant states originating from hole localization in different valleys. [7] These hydrogenic states can be observed in scanning tunneling spectroscopy (STS) but are, to a large degree, independent of the chemical origin of the defect, thus obscuring the chemical identification by its electronic fingerprint.

Here we unambiguously identify this common charged impurity defect as a carbon-hydrogen complex at a chalcogen site ($CH_X$) by comparing nominally undoped with intentionally carbon doped TMD samples. By a post-growth plasma-assisted process we could increase the CH impurity density by two orders of magnitude into the atomic percentage levels. In addition we confirm the assignment with atomically-resolved topographic and electronic structure measurements and *ab-initio* modeling. Our atomically-resolved scanning probe measurements demonstrate that the plasma treatment is selective, clean, and allows a high level of defect density control. The negative charge localization at CH impurities suggests that this defect can significantly affect the optoelectronic properties of TMDs. The detailed understanding of defect electronic properties, along with the controlled generation can be utilized to tailor TMD functionality by synthetic means.

## Results and Discussion

Three TMD samples were examined in this study: undoped tungsten diselenide ($WSe_2$), undoped tungsten disulfide ($WS_2$), and carbon doped $WS_2$. Monolayer islands of $WS_2$ and $WSe_2$ on graphene on silicon carbide (SiC) substrates were prepared by chemical vapor deposition (CVD) [26,27] and metalorganic chemical vapor deposition (MOCVD) [21,28] respectively. Figures 1(a) and (b) show typical scanning tunneling microscopy (STM) overview images of as-grown $WSe_2$ and $WS_2$ respectively, where a variety of intrinsic point defects can be observed. We have previously identified common defects in CVD-grown $WS_2$ to be oxygen at top and bottom chalcogen sites and chromium and molybdenum at tungsten sites. [15–17] Due to their very similar topography and local density of states as measured by CO-tip noncontact atomic force microscopy (nc-AFM) and scanning tunneling microscopy/spectroscopy (STM/STS) respectively, we identify $O_{Se}$ top and bottom, $Cr_W$ and $Mo_W$ also in $WSe_2$.

In all samples we observe a negatively charged defect, which we tentatively refer to as"nCD", that is imaged as a ∼2 nm dark depression at positive biases [as seen in figure 2(a)] and a protrusion at negative biases. This contrast inversion is due to strong upwards band bending in the proximity of the negatively charged defect [7,15]. The negative charge arises from the filling of a partially occupied valence band from the underlying graphene/SiC substrate, which acts as a Fermi sea [7,29]. Atomically-resolved CO-tip nc-AFM imaging [15, 30] indicates that this defect is located at a chalcogen site [see figure 2(b)]. The defect appears as a small repulsive feature, indicating that it is either smaller than a sulfur atom or resides closer to the tungsten plane. Conversely, figure 2(e) shows that the defect is either larger than or further away from the tungsten plane than a top oxygen substitution that was measured in the same image. Previously, we used density functional theory (DFT) to narrow down possible impurity candidates that are consistent with the experimentally observed atomic and electronic structure of nCD. Two possibilities remained: a carbon-hydrogen (CH) group or a nitrogen atom at a chalcogen site. [15]

To pinpoint the identity of the defect, we intentionally carbon doped $WS_2$ samples with an inductively coupled methane plasma-enhanced CVD process. [31] Previous results indicated that methane plasma treatment results in CH substituting for sulfur. [31] Figure 1(c) shows an overview image of a CH-doped sample using a 1 sccm flow of methane. A significant increase in nCD defect density is observed. The measured defect density of 0.6% is in excellent agreement with the expected value derived by linear extrapolation from higher methane flow rates. (Previously we observed that a 5 sccm flow rate resulted in a 3.3% carbon atomic percentage incorporation). The CH defect density is approximately two orders of magnitude higher than in the nominally undoped reference sample where we count 59 ppm. However, the nCD density between different undoped samples was found to strongly fluctuate from low parts per million to as much as parts per thousand levels (see supplementary material).

To confirm that the nCD defects in the intentionally doped sample are equivalent to the nCD defects on the pristine samples we compared their atomic contrast measured with CO-tip nc-AFM. As well, STS measurements [figure 3(a)] of the nCD defect in the undoped (blue) and doped (purple) sample show nearly identical resonances. The spectral features are rigidly shifted, which we attribute to the different Fermi level alignment of the substrates (see supplementary material). The resonance energies also strongly shift depending on the local environment as is observed in a selection of five different $CH_S$ dopants that are in close proximity to other negatively

charged defects, shown in figure 3(b). The energetic shift of up to $\sim 150\,\mathrm{meV}$ suggests a strong susceptibility to electrostatic gating effects [32]. When separated closer than $\sim 1\,\mathrm{nm}$ the STS features start to change indicating the formation of hybrid defect states. This is in agreement with previous photoluminescence studies that showed that increasing CH doping resulted in the detection of new emission states. [31]

The identification of the $CH_S$ impurity and the negative charge state is also confirmed by DFT calculations. Previously, [31] CH was found to be the most stable hydrocarbon substitution at a sulfur site, energetically more favorable than other conceivable fragments of the methane plasma such as $CH_3$, $CH_2$, or C. Our DFT calculations predict the binding energy of a CH impurity formed at a S site in the presence of free CH radicals and S vacancies to be -0.55 eV. Sulfur vacancies can be expected to be introduced during the plasma treatment because of the high temperature applied and admixed hydrogen to the plasma. The large energy gain results from the high reactivity of CH radicals and S vacancies. This confirms that CH incorporation in $WS_2$ (and similarly in other TMDs) is a likely high-temperature process amid hydrocarbon containing environments.

In figure 4 the calculated band structure of pristine monolayer $WS_2$ [4(a)] and $WS_2$ containing a $CH_S$ [4(b)] impurity is shown. The impurity introduces a defect state overlapping with occupied $WS_2$ states and depletes one electron from the $WS_2$ valence band, lowering the Fermi level of the isolated $WS_2$ slab, which is consistent with the previous calculation [31]. Upon electrical contact with the graphene substrate, this partially-occupied band will be filled, resulting in a negative charge localized at the defect site, consistent with experimental observations. The carbon $|j = 3/2, l = 1, m_j = \pm 1/2\rangle \equiv \psi_{C1}$ and hydrogen $|j = 1/2, l = 0, m_j = \pm 1/2\rangle \equiv \psi_H$ orbital contribution to the electronic states that arise due to the $CH_S$ defect are indicated with purple circles in figure 4(b). We find two defect states close to the band edges with significant contributions of $\psi_{C1}$ and $\psi_H$ states. These states exhibit bonding and anti-bonding character, in the occupied and unoccupied spectrum, respectively [see figures 4(c-f)]. Figures 4(c) and (e) display side projections of the electron density and figures 4(d) and (f) show a top view of the orbital isosurfaces. These bands contain not only CH contribution, but also $WS_2$ contribution, showing strong hybridization between CH and $WS_2$ upon the formation of $CH_S$. The carbon $|j = 3/2, l = 1, m_j = \pm 3/2\rangle \equiv \psi_{C2}$ contribution can be found mainly in the valence band edge of the $WS_2$, resulting from the formation of C-W bonds (see supplementary information).

In addition to the electronic properties, the calculated relaxed geometry was used to determine the structural changes of the $WS_2$ lattice upon incorporation of a CH impurity. The sulfur atom directly beneath the carbon atom moves away from the impurity by 118 pm, while the neighboring sulfur atoms in the top plane move closer. The three bonded tungsten atoms relax towards the sulfur atom below (see supplementary information). Using the relaxed geometry, we simulated the CO-tip nc-AFM image contrast, [33] shown in figure 2(c). In experiment, we observe a subtle protrusion at the position of the defect, in excellent agreement with the simulated image. This further confirms the identification of $CH_S$. Both the experimental and simulated images show a slight reduction of the sulfur-sulfur distances for the neighboring in-plane sulfur atoms (see supplementary information). This observed shortening is a convolution of the actual lattice contraction due to the defect and the effect of bending of the CO molecule at the tip apex. [34]

## Summary

In this work we use a combination of STM/STS, nc-AFM, *ab initio* DFT calculations, and targeted synthesis to unambiguously identify a carbon-hydrogen (CH) complex at a chalcogen site as a common, charged impurity in CVD-grown $WS_2$ and MOCVD-grown $WSe_2$. Even in nominally undoped samples we observed a wide range of CH impurity densities from $< 10^{10}\,\mathrm{cm}^{-2}$ to mid $10^{12}\,\mathrm{cm}^{-2}$ suggesting that carbon impurity defects in synthetic TMDs can be a considerable issue. Using a methane plasma treatment we could controllably increase the $CH_S$ density by two orders of magnitude to the atomic percentage range. The selectivity, cleanliness, and density control of post-synthetic TMD doping shown here demonstrates the promising prospects of tailoring TMD properties by surface chemistry.

## Methods

### *Sample Preparation*

$WSe_2$ growth: Metalorganic chemical vapor deposition (MOCVD) synthesis of tungsten diselenide (WSe2) was performed in a custom-built, vertical, cold-wall, gas-source CVD reactor. Tungsten hexacarbonyl [$W(CO)_6$, 99.99%, Sigma-Aldrich] and hydrogen selenide ($H_2Se$, 99.99%, Matheson) were used as metal and chalcogen precursors respectively in a hydrogen gas atmosphere, as previously reported. [21, 35, 36] A multistep growth method (nucleation, ripening, and lateral growth) was employed to synthesize $WSe_2$ on epitaxial graphene (EG) where the growth temperature and pressure were kept at constant 800°C and 700 Torr, respectively. [36] $W(CO)_6$ was kept in a stainless-steel bubbler where the bubbler temperature and pressure were always maintained at constant 30°C and 725 Torr. During the growth, $W(CO)_6$ flow rate was varied from $1.2\text{x}10^{-3}$ sccm to $2.7\text{x}10^{-4}$ sccm at the different growth stages while the $H_2Se$ flow rate was always kept at constant 7 sccm. The precursors were introduced from separate gas lines to prevent the intermixing before reaching the reactor inlet.

$WS_2$ Growth: Monolayer islands of tungsten disulfide ($WS_2$) were grown on graphene/SiC substrates with an ambient pressure CVD approach. [37–39] A graphene/SiC substrate with 10 mg of WO3 powder on top was placed at the center of a quartz tube, and 400 mg of sulfur powder was placed upstream. During synthesis, the furnace was heated to 900 °C and the sulfur powder was heated to 250 °C separately using a heating belt. Argon gas flow of 100 sccm was used as carrier gas throughout the process. The growth time was 60 min.

Carbon doping: An inductively coupled plasma-enhanced CVD system was used to carry out the post-growth CH doping. [31] The as-grown WS2/graphene/SiC was first placed at the hot zone of the furnace. Flows of 200 sccm of $Ar/H_2$ and 1 sccm of $CH_4$ were then introduced into the system, while radio frequency (13.56 MHz) was applied in order to generate the $CH_4/Ar/H_2$ plasma. During the treatment, the furnace temperature was increased incrementally to 400 °C and held for 15 minutes. Carbon doping was confirmed with Raman spectroscopy (see supplementary information).

After ex-situ growth, samples were transferred to ultrahigh vacuum ($< 2\text{x}10^{-10}$ mbar) and annealed at 200°C to remove adsorbates.

*Scanning Probe Microscopy (SPM) Measurements*

All SPM measurements were acquired with a Createc GmbH scanning probe microscope operating under ultrahigh vacuum ($p < 2\text{x}10^{-10}$ mbar) at liquid helium temperatures ($T < 7$ K). Measurements were taken with a focused ion beam cut platinum-iridium terminated quartz crystal cantilever (qPlus based) sensor [40]. Tip apexes were prepared by indentations into a gold substrate and verified as metallic on the Au(111) surface. Typical qPlus sensor parameters were a resonance frequency of $f_0 = 30$ kHz, spring constant of $k \sim 1800$ N/m, quality factor of $Q > 20{,}000$, and an oscillation amplitude of $A = 1$ Å. All noncontact atomic force microscopy (nc-AFM) images were obtained with a carbon monoxide (CO) functionalized tip [41] in constant height mode at zero bias. Scanning tunneling microscopy (STM) topographic measurements were taken in constant current mode with the bias applied to the sample. Scanning tunneling spectroscopic (STS) measurements were recorded using a lock-in amplifier with a resonance frequency of 683 Hz and a modulation amplitude between 2 and 10 mV.

*Density Functional Theory*

We performed first-principles density-functional theory (DFT) calculations using QUANTUM ESPRESSO package [42, 43]. We used the PBE generalized gradient approximation for exchange and correlation [44] with scalar and fully relativistic optimized norm-conserving Vanderbilt (ONCV) pseudopotentials from Pseudo Dojo library [45]. Spin-orbit coupling (SOC) is treated self-consistently for electronic structure calculations on top of the PBE geometry. We used the optimized lattice parameter of monolayer $WS_2$ of 3.192 Å with PBE and constructed $5 \times 5$ supercell to simulate an isolated $CH_S$ defect with $\sim$ 15 Å vacuum between adjacent slabs. We used a 100 Ry planewave cutoff energy and a gamma-centered $4 \times 4$ $k$-grid with Methfessel-Paxton smearing with a broadening of 0.02 Ry [46]. We investigated the energetics of $CH_S$ by calculating the binding energy ($E_b$) of $CH_S$. Here we define $E_b = E[CH_S] - E[CH] - E[Vac_S]$, where $E[CH_S]$, $E[CH]$, and $E[Vac_S]$ are total energies of $CH_S$, isolated CH molecule, and S vacancy without SOC, respectively.

## Acknowledgements

Scanning probe measurements were performed at the Molecular Foundry supported by the Office of Science, Office of Basic Energy Sciences, of the U.S. Department of Energy under Contract No. DE-AC02-05CH11231. This work was supported as part of the Center for Novel Pathways to Quantum Coherence in Materials, an Energy Frontier Research Center funded by the US Department of Energy, Office of Science, Basic Energy Sciences. K.C. was supported by the University of California - National Lab Collaborative Research and Training (UC-NL CRT) program. A.W.-B. was supported by the U.S. Department of Energy Early Career Award. B.S. appreciates support from the Swiss National Science Foundation under project number P2SKP2_171770. A.K. and J.R. acknowledge funding from Intel through the Semiconductor Research Corporation (SRC) Task 2746.001, the Penn State 2D Crystal Consortium (2DCC)-Materials Innovation Platform (2DCCMIP) under NSF cooperative agreement DMR1539916, and NSF CAREER Award 1453924. J.-H.L. and J.B.N. were supported by the Air Force Office of Scientific Research Hybrid

Materials MURI under award number FA9550-18-1-0480. Computational resources for performing the *ab initio* calculations were provided by the National Energy Research Scientific Computing Center. F.Z. and M.T. were supported by the Basic Office of Science of the Department of Energy under award DE-SC0018025. The authors thank Zhuohang Yu for technical support.

## References

[1] Chhowalla M, Shin H S, Eda G, Li L J, Loh K P and Zhang H 2013 *Nat. Chem.* **5** 263
[2] Manzeli S, Ovchinnikov D, Pasquier D, Yazyev O V and Kis A 2017 *Nat. Rev. Mater.* **2** 17033
[3] Yang J H and Yakobson B 2017 *arXiv:* 1711.05094
[4] Lin Z, Carvalho B R, Kahn E, Lv R, Rao R, Terrones H, Pimenta M A and Terrones M 2016 *2D Mater.* **3** 022002
[5] Aharonovich I, Englund D and Toth M 2016 *Nat. Photonics* **10** 631
[6] Qiu H, Xu T, Wang Z, Ren W, Nan H, Ni Z, Chen Q, Yuan S, Miao F, Song F *et al.* 2013 *Nat. Commun.* **4** 2642
[7] Aghajanian M, Schuler B, Cochrane K A, Lee J H, Kastl C, Neaton J B, Weber-Bargioni A, Mostofi A A and Lischner J 2019 *arXiv:* 1909.02320
[8] Wang Q H, Kalantar-Zadeh K, Kis A, Coleman J N and Strano M S 2012 *Nat. Nanotechnol.* **7** 699
[9] Wang H, Zhang C and Rana F 2015 *Nano Lett.* **15** 339–345
[10] Atallah T, Wang J, Bosch M, Seo D, Burke R, Moneer O, Zhu J, Theibault M, Brus L, Hone J *et al.* 2017 *J. Phys. Chem. Lett.* **8** 2148–2152
[11] Ye M, Seo H and Galli G 2019 *Npj Comput. Mater.* **5** 1–6
[12] Han H V, Lu A Y, Lu L S, Huang J K, Li H, Hsu C L, Lin Y C, Chiu M H, Suenaga K, Chu C W *et al.* 2016 *ACS Nano.* **10** 1454–1461
[13] Park J H, Sanne A, Guo Y, Amani M, Zhang K, Movva H C, Robinson J A, Javey A, Robertson J, Banerjee S K *et al.* 2017 *Sci. Adv.* **3** e1701661
[14] Jariwala D, Sangwan V K, Lauhon L J, Marks T J and Hersam M C 2014 *ACS Nano.* **8** 1102–1120
[15] Schuler B, Lee J H, Kastl C, Cochrane K A, Chen C T, Refaely-Abramson S, Yuan S, van Veen E, Roldan R, Borys N J *et al.* 2019 *ACS Nano.* **13** 10520–10534
[16] Schuler B, Qiu D Y, Refaely-Abramson S, Kastl C, Chen C T, Barja S, Koch R J, Ogletree D F, Aloni S, Schwartzberg A M *et al.* 2019 *Phys. Rev. Lett.* **123** 076801
[17] Barja S, Refaely-Abramson S, Schuler B, Qiu D Y, Pulkin A, Wickenburg S, Ryu H, Ugeda M M, Kastl C, Chen C *et al.* 2019 *Nat. Commun.* **10** 3382
[18] Addou R, Colombo L and Wallace R M 2015 *ACS Appl. Mater. Interfaces* **7** 11921–11929
[19] Le Quang T, Nogajewski K, Potemski M, Dau M T, Jamet M, Mallet P and Veuillen J 2018 *2D Mater.* **5** 035034
[20] Liu X, Balla I, Bergeron H and Hersam M C 2016 *J. Phys. Chem. C* **120** 20798–20805
[21] Lin Y C, Jariwala B, Bersch B M, Xu K, Nie Y, Wang B, Eichfeld S M, Zhang X, Choudhury T H, Pan Y *et al.* 2018 *ACS Nano.* **12** 965–975
[22] Ghorbani-Asl M, Enyashin A N, Kuc A, Seifert G and Heine T 2013 *Phys. Rev. B* **88** 245440
[23] Tongay S, Suh J, Ataca C, Fan W, Luce A, Kang J S, Liu J, Ko C, Raghunathanan R, Zhou J *et al.* 2013 *Sci. Rep.* **3** 1–5
[24] Yu Z, Pan Y, Shen Y, Wang Z, Ong Z Y, Xu T, Xin R, Pan L, Wang B, Sun L *et al.* 2014 *Nat. Commun.* **5** 5290
[25] Carozo V, Wang Y, Fujisawa K, Carvalho B R, McCreary A, Feng S, Lin Z, Zhou C, Perea-López N, Elías A L *et al.* 2017 *Sci. Adv.* **3** e1602813
[26] Elías A L, Perea-López N, Castro-Beltrán A, Berkdemir A, Lv R, Feng S, Long A D, Hayashi T, Kim Y A, Endo M *et al.* 2013 *ACS Nano.* **7** 5235–5242
[27] Kastl C, Chen C T, Kuykendall T, Shevitski B, Darlington T P, Borys N J, Krayev A, Schuck P J, Aloni S and Schwartzberg A M 2017 *2D Mater.* **4** 021024
[28] Eichfeld S M, Hossain L, Lin Y C, Piasecki A F, Kupp B, Birdwell A G, Burke R A, Lu N, Peng X, Li J *et al.* 2015 *ACS Nano.* **9** 2080–2087
[29] Brotons-Gisbert M, Branny A, Kumar S, Picard R, Proux R, Gray M, Burch K S, Watanabe K, Taniguchi T and Gerardot B D 2019 *Nat. Nanotechnol.* **14** 442
[30] Gross L, Mohn F, Moll N, Liljeroth P and Meyer G 2009 *Science* **325** 1110

[31] Zhang F, Lu Y, Schulman D S, Zhang T, Fujisawa K, Lin Z, Lei Y, Elias A L, Das S, Sinnott S B *et al.* 2019 *Sci. Adv.* **5** eaav5003
[32] Raja A, Chaves A, Yu J, Arefe G, Hill H M, Rigosi A F, Berkelbach T C, Nagler P, Schüller C, Korn T *et al.* 2017 *Nat. Commun.* **8** 1–7
[33] Hapala P, Kichin G, Wagner C, Tautz F S, Temirov R and Jelínek P 2014 *Phys. Rev. B.* **90** 085421
[34] Gross L, Mohn F, Moll N, Schuler B, Criado A, Guitián E, Peña D, Gourdon A and Meyer G 2012 *Science* **337** 1326–1329
[35] Kozhakhmetov A, Nasr J R, Zhang F, Xu K, Briggs N C, Addou R, Wallace R, Fullerton-Shirey S K, Terrones M, Das S *et al.* 2019 *2D Mater.* **7** 015029
[36] Zhang X, Choudhury T H, Chubarov M, Xiang Y, Jariwala B, Zhang F, Alem N, Wang G C, Robinson J A and Redwing J M 2018 *Nano Lett.* **18** 1049–1056
[37] Giusca C E, Rungger I, Panchal V, Melios C, Lin Z, Lin Y C, Kahn E, Elías A L, Robinson J A, Terrones M *et al.* 2016 *ACS nano* **10** 7840–7846
[38] Ulstrup S, Giusca C E, Miwa J A, Sanders C E, Browning A, Dudin P, Cacho C, Kazakova O, Gaskill D K, Myers-Ward R L *et al.* 2019 *Nature communications* **10** 1–7
[39] Kastl C, Chen C, Koch R, Schuler B, Kuykendall T, Bostwick A, Jozwiak C, Seyller T, Rotenberg E, Weber-Bargioni A *et al.* 2018 *2D Materials* **5** 045010
[40] Giessibl F J 1998 *Appl. Phys. Lett.* **73** 3956
[41] Mohn F, Schuler B, Gross L and Meyer G 2013 *Appl. Phys. Lett.* **102** 073109
[42] Giannozzi P, Baroni S, Bonini N, Calandra M, Car R, Cavazzoni C, Ceresoli D, Chiarotti G L, Cococcioni M, Dabo I *et al.* 2009 *J. Phys.: Condens. Matter* **21** 395502
[43] Giannozzi P, Andreussi O, Brumme T, Bunau O, Nardelli M B, Calandra M, Car R, Cavazzoni C, Ceresoli D, Cococcioni M *et al.* 2017 *J. Phys.: Condens. Matter* **29** 465901
[44] Perdew J P, Burke K and Ernzerhof M 1996 *Phys. Rev. Lett.* **77**(18) 3865–3868
[45] Hamann D R 2013 *Phys. Rev. B* **88** 085117
[46] Methfessel M and Paxton A T 1989 *Phys. Rev. B* **40**(6) 3616–3621

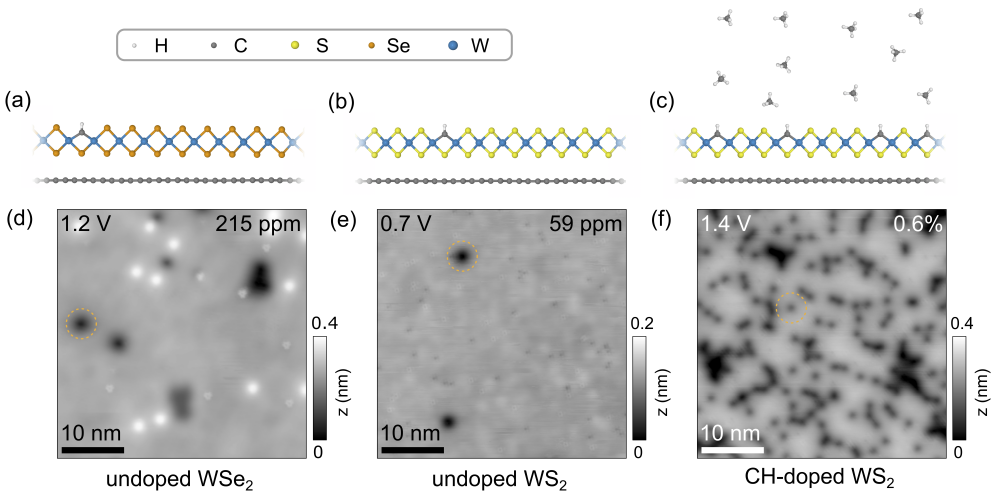


**Figure 1.** (a-c) Structural model of $WSe_2$ on graphene with one $CH_{Se}$ defect (a), $WS_2$ with one $CH_S$ defect and methane-plasma treated $WS_2$ with many $CH_S$ defects. (d) STM topographic overview image ($V_B = 1.2\,V$, $I_t = 100\,pA$) of undoped MOCVD $WSe_2$ showing a variety of point defects, including negatively charged defects (nCDs) that are observed as dark depressions (orange circle). (e) STM topography ($V_B = 0.7\,V$, $I_t = 100\,pA$) of undoped CVD-grown $WS_2$. (f) STM topography ($V_B = 1.4\,V$, $I_t = 100\,pA$) of methane plasma treated, CVD-grown $WS_2$. An increased concentration of dark defects is observed in the carbon doped sample. Here we identify these dark defects as CH substituting for a chalcogen atom. The defect densities are indicated in the top right corner.

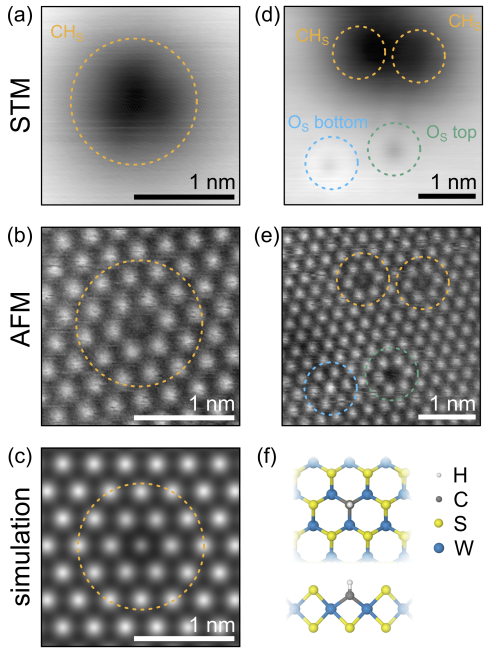


**Figure 2.** (a) STM ($V_b$ = 1.2 V, $I_t$ = 100 pA) image of an isolated CH in sulfur site defect ($CH_S$) in CH-doped $WS_2$. (b) CO-tip nc-AFM image of the same $CH_S$ defect as in (a). Sulfur atoms in the upper S layer are imaged as bright protrusions. (c) Simulated nc-AFM image of $CH_S$ using the calculated DFT geometry and the probe particle method [33]. (d) STM ($V_b$ = 1.2 V, $I_t$ = 100 pA) and (e) nc-AFM images of two $CH_S$ (orange circles), an $O_S$ top (green circle) and $O_S$ bottom (blue circle) defect in CH-doped $WS_2$. (f) Top and side view of the DFT calculated structural model of $CH_S$.

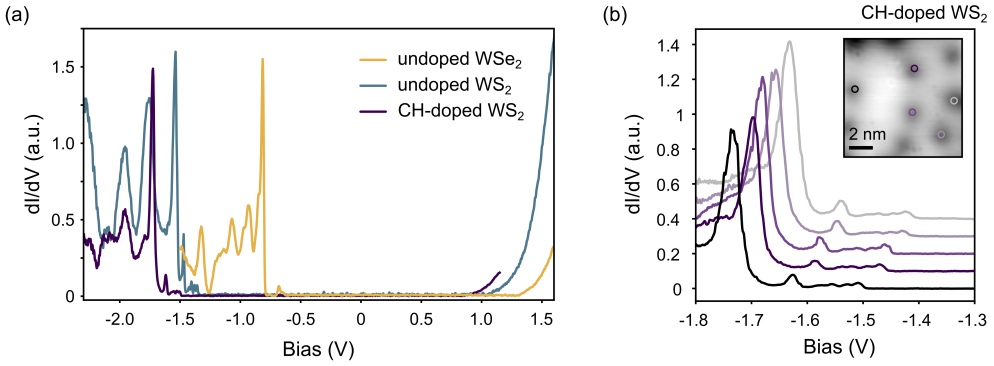


**Figure 3.** (a) Scanning tunneling spectroscopy (STS) of a $CH_S$ defect in undoped $WSe_2$ (yellow), undoped $WS_2$ (blue), and CH-doped $WS_2$ (purple). The spectral features of the carbon impurity in both the doped and undoped $WS_2$ samples are very similar, but shifted in energy. (b) STS of several CH impurities in doped $WS_2$ (see STM inset) show a significant upwards shift of spectral features in proximity to other negatively charged defects.

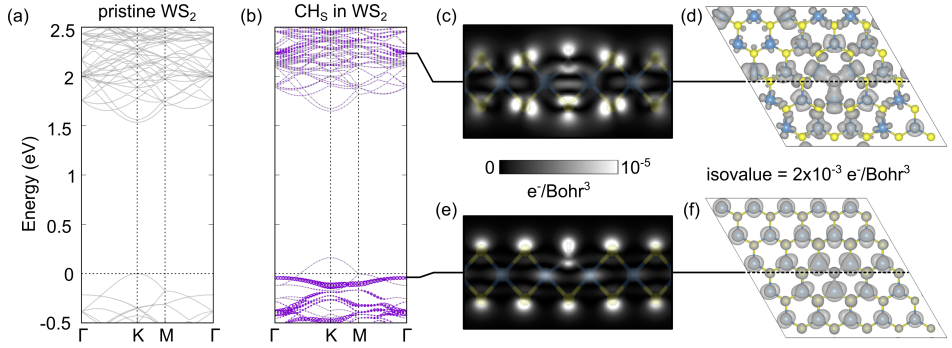


**Figure 4.** DFT band structure of (a) pristine $WS_2$ and (b) a CH substituting sulfur in $WS_2$. The zero in energy represents Fermi level. The purple circles indicate $|\psi_{C1}\rangle + |\psi_H\rangle$ contribution that form an anti-bonding (c anf d) and bonding (e and f) states at positive and negative energies, respectively. The size of circles is proportional to the weight of the $|\psi_{C1}\rangle + |\psi_H\rangle$. (c) and (e) show side projections of the electron density at the axis through the central $CH_S$ defect of the antibonding (c) and bonding (e) orbitals respectively. (d) and (f) show isosurfaces of the antibonding and bonding orbitals respectively from a top projection with a isovalue of $2x10^{-3}$ e$^-$/Bohr$^3$.